nature communications

Article

https://doi.org/10.1038/s41467-026-70568-z

Decoupling electronic and geometric effects in Pd catalysts via thermal surface reconstruction for selective hydrogenation

Received: 4 November 2025

Accepted: 28 February 2026

Published online: 18 March 2026

Check for updates

Minghang Li, Zhaoyuan Fu, Qian Luo, Bing Lu, Liwei Zhang, Shipan Liang, Ting Liu, Yong Wang & Shanjun Mao

The entangled electronic and geometric effects in heterogeneous catalysis have long obscured precise attribution of their individual roles. By employing a thermal-induced surface reconstruction strategy to progressively enhance metal-support interactions, we achieve continuous tuning of Pd's electronic and geometric structures. Using alkyne semi-hydrogenation as a prototypical structure-sensitive probe reaction, we demonstrate that despite the linear coupling of electronic and geometric structures during Pd reconstruction, the turnover frequency scales solely with the geometric descriptor W (quantifying Pd particle flattening), while selectivity regulation bifurcates into two distinct regimes: Below a critical W, electron-deficient Pd sites offset geometric constraints, yielding a non-structure-sensitive selectivity plateau; whereas above this threshold, electron-rich surfaces establish unequivocal geometric control. Moreover, surface reconstruction drastically shrinks the electronic-geometric space of Pd sites for over-hydrogenation side reaction. These insights provide a blueprint for metal catalysts regulation in hydrogenation and may open avenues for quantifying electronic-geometric interplay in other structure-sensitive reactions.

It is well known that the structure of a catalyst determines its performance. Due to the structural complexity of supported metal catalysts, the exploration of structure-performance relationships has long been a focal point in this field. For supported metal catalysts, reconstruction has been widely recognized as an effective means to adjust the catalytic performance[1–6]. Among them, researchers paid special attention to the redispersion of noble metal sites, as it can transform metal nanoparticles into sub-nanometer or even single-atom sites and regenerate sintered catalysts[7–10]. Regeneration methods include the redox method, oxychlorination, halogenated hydrocarbon heat treatment, etc., and are applicable to a wide range of noble metals such as Pt, Pd, Ru, Rh, and Au[11–14]. For example, alternating H_2/O_2 cycling treatments of Pd/FeO_x catalysts enabled reversible aggregation and redispersion of Pd species, driven by redox-responsive migration and anchoring at surface defect sites[15]. For oxychlorination, sintered $Pt–Re/Al_2O_3$ catalysts treated with 1,2-dichloropropane in air followed by H_2 reduction triggered significant recovery of Pt dispersion and catalytic performance[14]. Sintered Au/activated carbon treated with CH_3X (X = Cl, Br, I) at mild temperatures also resulted in the formation of volatile Au complexes and the redispersion of large gold particles into clusters smaller than 3 nm, thereby restoring catalytic activity in acetylene hydrochlorination[16]. Predominantly, the mechanism of redispersion is similar and can be explained with the 'strain model' in most cases, in which metal oxidation is believed to be a prerequisite factor to induce dispersion[17–19]. More detailed theoretical research indicated that such redispersion occurs only when the Gibbs free energy of disintegration (ΔG_{NP}^{dis}) is negative[20]. As a typical catalyst system, a series of interesting results for CeO_2-supported noble metal

Advanced Materials and Catalysis Group, Zhejiang Key Laboratory of Low-Carbon Synthesis of Value-Added Chemicals, State Key Laboratory of Clean Energy Utilization, Institute of Catalysis, Department of Chemistry, Zhejiang University, Hangzhou, P. R. China. e-mail: chemwy@zju.edu.cn; maoshanjun@zju.edu.cn

catalysts were reported recently, such as temperature-dependent redispersion routes, hydroxyl groups acting as the main anchoring sites to stabilize and disperse metal atoms and the entropy effect of metal redispersion[21–25].

Despite decades of research into these schemes, the majority of efforts have predominantly concentrated on the redispersion of metallic active components[26–29]. The study on the meticulous modulation of the morphology and electronic structure of these metallic active constituents on purpose along redispersion has been very limited since. A plethora of studies have reported that the orbital energy levels of metallic nanoparticles (NPs) can undergo splitting, or even transform into discrete molecular orbitals, as a result of alterations in their geometric configurations[30,31]. Compounding this complexity is the non-uniform conduction of electronic effects across metallic NPs, leading to a robust coupling between electronic and geometric effects[32]. Consequently, there remains a dearth of systematic quantitative assessment regarding the interplay between structural and catalytic properties of surface-reconstructed catalysts during reaction processes[33–37]. For instance, in structure-sensitive reactions like alkyne semi-hydrogenation, although studies have reported multiple kinds of structure-performance relationships, such as over-hydrogenation on low-coordinated sites and the so-called energy linear scaling relationships, there is still no systematic study on the respective influence weights of geometric and electronic effects during the reconstruction process. Although we previously decoupled and relatively quantified the electronic and geometric effects in the dehalogenation side reaction of halogenated nitrobenzene hydrogenation by combining morphology control of Pt NPs and work function modulation of supports, it is not applicable to the Pd catalyst system[32]. The main reason we found is that the change of the electronic structure of Pd sites on different supports prepared using the above method is not significant. By altering operating temperatures and atmospheres, it is theoretically possible to precisely control the structural evolution of the active phase and optimize the catalytic performance. Hence, analyzing the geometric and electronic effects of Pd catalyst systems in selective hydrogenation reactions through surface reconstruction may offer a viable solution. Consequently, there is an urgent need to develop simple yet controllable methods for catalyst surface reconstruction, along with appropriate research protocols to achieve these goals.

In this work, we effectively modulated the microstructure and coordination environment of active sites on Pd/CeO_2 catalysts through a thermal-induced surface reconstruction method. Systematic characterization and first-principles molecular dynamics simulations revealed that the surface reconstruction of the active phase resulted in the formation of uniformly dispersed, flattened Pd nanostructures with an aspect ratio significantly deviated from 1. Simultaneously, the interfacial $Pd^{\delta+}$ species increased, significantly boosting metal-support interactions. This thermally induced surface reconstruction of Pd/CeO_2 was driven by both the calcination atmosphere and the lattice oxygen of CeO_2. And the extent of surface reconstruction diminished with the increasing size of Pd NPs. Further, we correlated the thermally induced surface reconstruction with reaction performance in the selective hydrogenation of 2-methyl-3-butyn-2-ol (MBY), quantifying the structure-performance relationship. A linear scaling relationship was established between the aspect ratio (W value) of the Pd active phase and the hydrogenation activity of MBY. A two-stage influence interval on olefin selectivity was also identified for electronic and geometric effects. Using matrix transformation and grid interpolation, we created $Pd^{\delta+}$–W–Sel. contour plots to visualize the structure–activity relationship for alkyne semi-hydrogenation over Pd/CeO_2 catalysts, establishing clear design principles for catalyst optimization. The optimal Pd/CeO_2-500 catalyst, prepared with Pd salt as a precursor, exhibited exceptional reactivity (7291 h^{-1}) and over 96% selectivity of 2-methyl-3-buten-2-ol (MBE) without any poisoning agents, significantly outperforming the uncalcined counterpart and the commercial Lindlar catalyst (TOF = 401 h^{-1}, selectivity = 93.5%)[38,39]. Selectivity for MBE can be further improved to over 97.5% with Pd nanocrystals as precursors. The facile thermal-induced surface reconstruction method provides new insights into the quantitative study of structure–performance relationships on supported metal catalysts and the design of efficient catalysts.

Results and discussion

Structural evolution of surface-reconstructed Pd nanocatalysts

Supported Pd catalysts on commercial CeO_2 were synthesized via a simple wet impregnation strategy, followed by calcination in static air at different temperatures (see Experimental section for details) and sequential reduction in hydrogen at 200 °C. The samples were labeled as Pd/CeO_2-T_{calc}, where T_{calc} denotes the calcination temperature. Inductively coupled plasma mass spectrometry (ICP-MS) confirmed similar Pd contents (~0.5 wt%, Supplementary Table 1) across samples, consistent with the nominal metal loading. Various characterizations were used to disclose the structural evolution of Pd/CeO_2 nanocatalysts induced by air calcination. N_2 adsorption-desorption isotherm analysis showed minimal changes in specific areas after Pd species deposition (Supplementary Fig. 1)[40]. High-resolution transmission electron microscopy (HRTEM) images of uncalcined Pd/CeO_2 showed relatively large Pd NPs with an average size of 5.01 nm and uneven size distribution (Fig. 1a). Lattice fringes of 0.224 and 0.312 nm, corresponding to Pd (111) and CeO_2 (111) *d*-spacings, respectively, were observed in the top-view images (Supplementary Fig. 2)[41,42]. Pulse CO chemisorption provided quantitative measurements of the exposed metal surface area after calcination[43]. The results clearly showed a 3.2-fold increase in surface Pd atoms on Pd/CeO_2-500, with Pd dispersion increasing from 17.5% to 57.1%, consistent with TEM observations (Supplementary Table 1). Further extending the treatment time and increasing the calcination temperature resulted in negligible changes in Pd structure, as shown in Supplementary Fig. 3. H_2 temperature-programmed reduction (H_2-TPR) elucidated the distribution of Pd species and the metal–support interactions in Pd/CeO_2-T_{calc} catalysts (Fig. 1d). A negative peak around 90 °C (blue region) is typically attributed to the decomposition of Pd hydride (β-PdH_x)[44,45]. As the calcination temperature increased, the TPR curves showed a significant reduction in the peak intensity of β-PdH_x, indicating an increasing Pd dispersion. For the Pd/CeO_2-500 sample, the β-PdH_x negative peak almost disappeared, consistent with the high Pd dispersion (57.1%) observed in CO titration[46,47]. Accordingly, the increased reduction peak in the range of 250–300 °C indicated that the decreased β-PdH_x transformed to surface $Pd^{\delta+}$ species. Energy-dispersive X-ray spectroscopy (EDS) mapping further confirmed the uniform distribution of Pd in the reconstructed catalyst (Supplementary Fig. 4). These phenomena demonstrated that the metal–support interactions between Pd species and CeO_2 were significantly strengthened after heat treatment, further demonstrating the impact of high-temperature calcination on catalyst structure and properties.

During the gradual decrease in Pd particle size, we also observed a synchronous evolution of their morphology (Fig. 1a–c). The aspect ratio (denoted as W) of nanoparticles was used to quantify the morphology of Pd species. The W value is defined as the ratio of the shortest diameter (R1) to the longest diameter (R2) of the two-dimensional projection of Pd clusters, characterizing the degree of particle deformation (Fig. 1e). In the unannealed Pd/CeO_2 sample, directly reduced Pd NPs were quasi-spherical with a W value as high as 0.88. However, as the calcination temperature increased from 200 °C to 500 °C, Pd species gradually evolved from spherical to fish-scale-like nanostructures, with the W value significantly decreasing to 0.64 (Supplementary Figs. 5, 6). This wetting growth suggests tighter binding between Pd NPs and CeO_2, the increase of the proportion of interfacial sites and enhanced interfacial electron transfer, which is expected to improve the catalyst stability[48].

https://doi.org/10.1038/s41467-026-70568-z

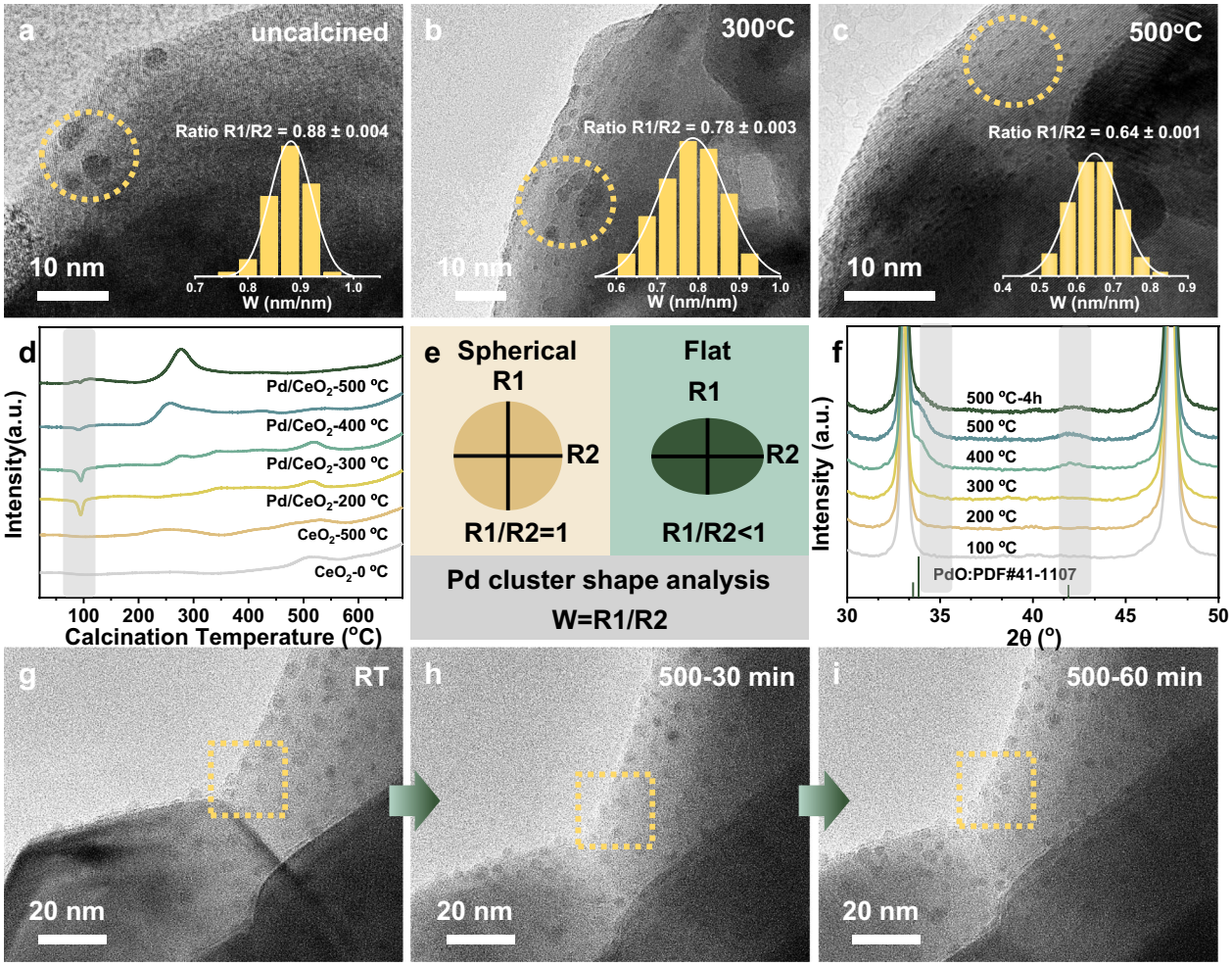

Fig. 1 | Surface structure evolution of heat-activated Pd/CeO_2 catalysts. **a**–**c** HRTEM images of Pd/CeO_2-T_{calc} (0, 300, 500 °C) series catalysts. Insets show the diameter ratio (W) distribution histograms of Pd. **d** H_2-TPR profiles of as-prepared Pd/CeO_2 catalysts. **e** Schematic presentation of the diameter ratio of the Pd nanoclusters based on the HRTEM images. **f** In situ XRD spectra of Pd/CeO_2 during programmed warming in air. **g**–**i** In situ environmental TEM images of $Pd_{NP\text{-}3.7}$/CeO_2 in oxygen atmosphere.

To more intuitively observe the structural evolution induced by thermal treatment, Pd NPs with an average diameter of 3.7 nm were supported on CeO_2 ($Pd_{NP\text{-}3.7}$/CeO_2). Then, the dynamic migration and morphological changes of Pd species were monitored with in situ environmental transmission electron microscopy (ETEM) (Fig. 1g–i). Prior to the initiation of calcination, electron microscopy images revealed that the supported Pd NPs largely retained their original size distribution. After more than 30 min of air treatment at 500 °C, the Pd NPs gradually fragmented into a greater number of smaller particles. This dynamic change clearly demonstrates that the Pd species undergo a process of particle fragmentation and redispersion under high-temperature oxidative conditions, leading to a more uniform distribution of the Pd active phase, rather than through a mechanism of vapor-phase migration of metal atoms under high calcination temperatures[48,49]. Furthermore, this study suggests that such thermally induced Pd site reconstruction may not be limited to specific metal precursors.

Mechanism of surface reconstruction in Pd nanocatalysts

The previous experimental results clearly demonstrated the basic reconstruction process of Pd species on CeO_2 support. However, further research is necessary on the physicochemical mechanisms that leave behind. Since surface reconstruction induced by calcination occurs in an air atmosphere, the catalyst precursor impregnated with metal salts may transform into PdO during the calcination process[50,51]. Subsequently, the PdO NPs are redispersed on supports along with processes such as fragmentation, deformation, migration, etc. Therefore, the oxygen source may play an important role in the reconstruction of Pd species during the calcination process.

To verify the above hypothesis, in situ temperature-programmed XRD was conducted to characterize the structure evolution of the catalyst precursor impregnated with $PdCl_2$ and the reduced Pd_{NP}/CeO_2 catalyst without air calcination. Considering that the previous Pd loading was relatively low (~0.5 wt%, Supplementary Fig. 7), the theoretical Pd loading was deliberately increased to 10 wt % in order to capture the evolution signal of Pd species during the reconstruction process (Supplementary Fig. 8). As shown in Fig. 1f, during the calcination process, the catalyst precursor impregnated with $PdCl_2$ firstly transformed into PdO phase, and then the peak intensity of PdO underwent a process from weak to strong and then disappeared. Correspondingly, the half peak width of PdO underwent a process of broadening to narrowing and then widening again[52]. This indicated that PdO continued to fragment into smaller pieces on CeO_2 after the complete conversion of $PdCl_2$ to PdO. Similarly, the metallic Pd particles in the uncalcined reduced Pd_{NP}/CeO_2 catalyst were firstly oxidized to PdO during air calcination, and then PdO underwent the same reconstruction process as the catalyst precursor (Supplementary Fig. 9). The above results clearly

https://doi.org/10.1038/s41467-026-70568-z

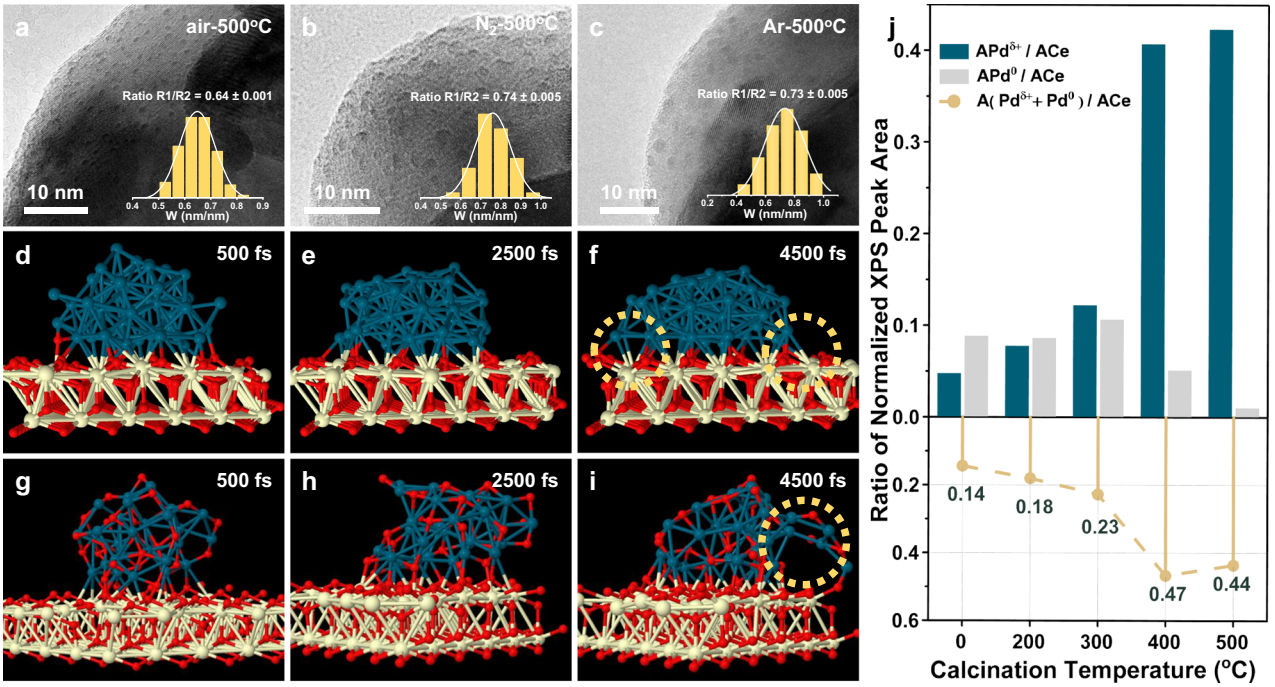

Fig. 2 | Mechanism for Pd reconstruction on CeO_2. a–c Representative HRTEM images of as-prepared Pd/CeO_2 samples calcined at 500 °C in different atmospheres: **a** Pd/CeO_2-air, **b** Pd/CeO_2-N_2, and **c** Pd/CeO_2-Ar. The inset shows the diameter ratio (W) distribution histograms of Pd. **d–i** Atomic models from AIMD simulations at 800 K with side views from 0 to 4500 fs. **d–f** Snapshots of Pd NPs; **g–i** snapshots of PdO NPs. **j** Thermal evolution of Pd species monitored by XPS. All XPS intensities relative to Ce 3*d*.

demonstrate that oxygen species are indeed involved in the reconstruction process of Pd catalysts.

However, two oxygen sources existed in the process of catalyst preparation: gaseous oxygen in air and lattice oxygen in CeO_2[53]. To further analyze the respective effects of the two oxygen sources, an inert atmosphere was applied to synthesize Pd/CeO_2-500-N_2 and Pd/CeO_2-500-Ar catalysts for comparison (Fig. 2a–c). High-resolution transmission electron microscopy (HRTEM) results showed that the W values of Pd NPs were determined to be 0.74 and 0.73, respectively. Compared with the W value of the uncalcined Pd/CeO_2 catalyst (0.88), the results indicated that Pd species on CeO_2 can still undergo reconstruction process even without the involvement of gaseous oxygen, albeit to a lesser extent than in air calcination, highlighting the critical role of both gas oxygen and lattice oxygen in Pd structural evolution, consistent with the proposed mechanism involving fragmentation, deformation and migration of PdO. Ab initio molecular dynamics (AIMD) simulations further supported the structural evolution of Pd species at the atomic level (Supplementary Figs. 10, 11). Simulations under inert atmospheres showed that atoms on Pd NPs with a typical Wulff structure gradually migrated to the surface of CeO_2 to bind with surface lattice oxygen and formed flatter nanostructures with significantly reduced W values as indicated by yellow circles in Fig. 2d–f when calcination time was increased from 500 to 4500 fs. Under oxygen atmospheres, PdO formed by the oxidation of Pd NPs flattened faster at the same temperature (Fig. 2g–i), with more Pd atoms binding to the CeO_2 support and higher interfacial wetting.

It is worth noting that since Pd NPs tend to have more Pd atoms interacting with the support during flattening, it is reasonable to assume that the driving force for Pd nanoparticle flattening is the difference between Pd–support and Pd–Pd interactions[54,55]. Stronger interactions generally implied more electron transfer. To verify this, we tracked the electronic structure of Pd species during the evolution of Pd/CeO_2-T_{calc} using X-ray photoelectron spectroscopy (XPS). As shown in Fig. 2j, the peak intensity of the Pd 3*d* core-level spectra significantly increased with the rise of the calcination temperature, which is consistent with the above conclusion of an improved dispersion of Pd NPs on the catalyst surface[56–58]. Fine analysis of the Pd 3*d* spectra of Pd/CeO_2-T_{calc} samples showed that Pd^0 species with a binding energy of 335.5 eV dominated in uncalcined and low-temperature calcined samples. As the calcination temperature increased, the ratio of Pd^0 gradually diminished. Meanwhile, the concentration of electron-deficient interfacial $Pd^{\delta+}$ species at 337.8 eV rose sharply. For Pd/CeO_2-500, the ratio of $Pd^{\delta+}$ even accounted for 97.6%, in alignment with the H_2-TPR results in Fig. 1d, further confirming the synchronous transformation of oxidation state and coordination environment during the structural evolution of Pd sites. Surely, the increase in interfacial $Pd^{\delta+}$ species also indicates enhanced electronic interactions between the CeO_2 support and Pd NPs after thermally induced structural changes. In addition, peak fitting of the high-resolution O 1*s* core-level spectra of Pd/CeO_2-T_{calc} catalysts demonstrated that the ratio of oxygen vacancies (BE = 532.2 eV) also increased from 27.6% to 45.6% as the calcination temperature increased to 500 °C (Supplementary Fig. 12)[47]. Since the reduction condition is the same for all the Pd/CeO_2-T_{calc} catalysts, it is reasonable to speculate that lattice oxygen participates in the surface reconstruction of Pd sites through forming numerous $Pd^{\delta+}$ interfacial structures, which finally results in an elevated concentration of oxygen vacancies[59].

Since the oxygen activity varies among different supports, this difference is expected to affect the degree of Pd reconstruction. Therefore, the reconstruction behavior of Pd NPs was further explored on supports with different properties. Specifically, colloidal Pd NPs with an average size of about 2.9 nm and a W value of about 0.91 were deposited on TiO_2, SiO_2, Al_2O_3, and MgO carriers, followed by $NaBH_4$/tert-butylamine treatment to remove the capping agent polyvinyl pyrrolidone (PVP)[32]. A series of Pd NPs-supported nanocatalysts was then prepared (Supplementary Figs. 13, 14). Air calcination was then used to induce Pd surface reconstruction. Results showed that significant structural changes, like dispersion and shape, occurred on Pd species supported on reducible supports like CeO_2 and TiO_2. For instance, the average size of Pd NPs for Pd_{NP}/TiO_2-500 decreased from

https://doi.org/10.1038/s41467-026-70568-z

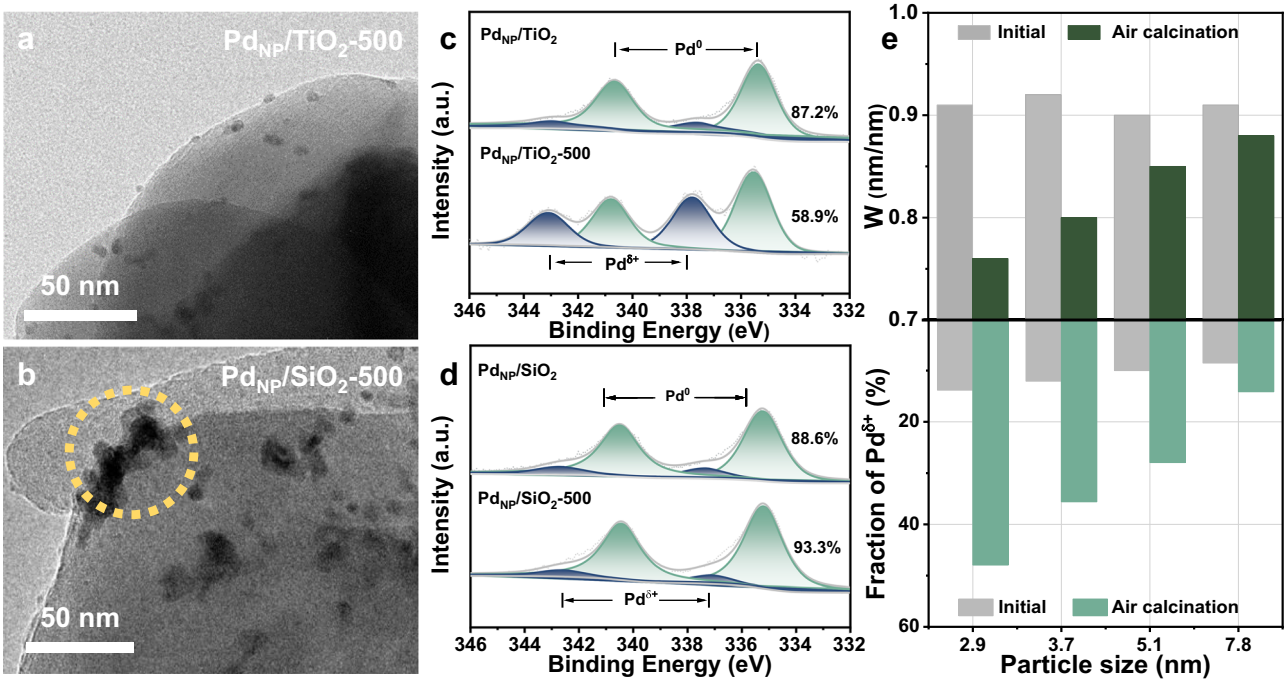

Fig. 3 | Influence of supports for Pd reconstruction. HRTEM images of **a** Pd_{NP}/TiO_2 and **b** Pd_{NP}/SiO_2 nanocatalysts after air calcination at 500 °C. High-resolution XPS spectra of Pd 3*d* specimens for $Pd_{NP\text{-}2.9}/TiO_2$ **c** and $Pd_{NP\text{-}2.9}/SiO_2$ **d** nanocatalysts before and after air calcination. **e** Comparison of the $Pd^{\delta+}$ interfacial content and the W values of Pd_{NP}/CeO_2 catalysts before and after reconstruction.

2.95 nm to 2.52 nm, along with the W value reducing from 0.92 to 0.81 (Fig. 3a, Supplementary Fig. 15). In contrast, air calcination treatment caused serious sintering and agglomeration of Pd NPs with no significant redispersion observed on non-reducible supports (e.g., SiO_2, Al_2O_3, and MgO) (Supplementary Fig. 16)[60]. XPS characterization of $Pd_{NP\text{-}2.9}/TiO_2$ and $Pd_{NP\text{-}2.9}/SiO_2$ catalysts before and after air calcination further showed that the electron-rich Pd^0 content in reconstructed Pd_{NP}/TiO_2-500 catalyst decreased from 87.2% to 58.9% (Fig. 3c), along with the electron-deficient Pd–O–Ti species rapidly increased from 12.8% to 41.1% correspondingly[61], indicating similarly enhanced interaction between Pd active sites and support as the case for Pd/CeO_2. In contrast, due to the sintering caused by air calcination, the Pd^0 content in reconstructed Pd_{NP}/SiO_2-500 actually increased by 4.7% (Fig. 3b, d). Hence, the activity to form oxygen vacancies is critical for lattice oxygen to induce the reduction of Pd.

Additionally, the reconstruction behavior of Pd NPs of different sizes on reducible supports also showed significant differences (Supplementary Figs. 17–20, Table 2). HRTEM analysis of the calcined catalysts revealed that the average W value for samples with small-sized Pd NPs, such as $Pd_{NP\text{-}2.9}/CeO_2$-500, decreased from 0.91 to 0.75 (Fig. 3e). The W change amplitude reached 17.6%, indicating a significant deformation of Pd sites after calcination. However, samples with large-sized Pd NPs, such as $Pd_{NP\text{-}7.8}/CeO_2$, showed only a 3.3% decrease in average W value (from 0.91 to 0.88) after calcination. These results suggest that the thermally induced reconstruction effect gradually diminishes with the rise of the size of Pd NPs (Supplementary Fig. 21). This particle size sensitivity of the reconstruction effect was also confirmed by XPS results of the catalysts. As shown in Fig. 3e, the ratio of Pd^0 remained at about 85–90% in the series of Pd_{NP}/CeO_2 catalysts with minimal change in W values, typically involving an initial size varying from 3.0 nm to 7.8 nm for colloidal Pd NPs. In contrast, the Pd^0 content in the apparent reconstructed series significantly decreased (52.1–85.8%), typically involving an initial size varying from 2.2 to 7.7 nm for colloidal Pd NPs, indicating more prevalent Pd–O–Ce structures and enhanced interaction between Pd sites and CeO_2. Similarly, the modulation of the electronic structure of Pd NPs also gradually faded through thermally induced reconstruction as the average size of colloidal Pd NPs increased.

To summarize, both experimental characterizations and theoretical calculations revealed that oxygen in the air and lattice oxygen in reducible supports jointly participated in promoting the reconstruction of the Pd active phase, forming flattened Pd structures and enhanced Pd–support interfacial interactions.

Catalytic performance of surface-reconstructed pd nanocatalysts in alkyne semi-hydrogenation

Next, the impact of Pd reconstruction on the catalytic performance was studied in Pd/CeO_2-T_{calc} series catalysts, using the structure-sensitive reaction of alkyne semi-hydrogenation as an example.

As shown in Fig. 4a, the activity positively correlated with the calcination temperature within the 200–500 °C range. The optimal Pd/CeO_2-500 catalyst displayed 2.35 times higher apparent catalytic activity for MBY semi-hydrogenation compared to the uncalcined one. Since air calcination causes the redispersion of Pd sites, the increase in apparent hydrogenation activity is expected. Surprisingly, the TOF value (7291 h^{-1}) for MBY hydrogenation on the optimal Pd/CeO_2-500 catalyst was 57% higher than that of the uncalcined one (4640 h^{-1}) (Supplementary Fig. 22). This improvement in intrinsic activity indicates that the enhanced catalytic activity of Pd/CeO_2-T_{calc} catalysts is not solely due to the increased number of Pd sites. Further increasing the calcination temperature to 600 °C, the catalytic performance of Pd/CeO_2-600 began to decline, likely due to slight sintering of the CeO_2 carrier (Supplementary Fig. 23), reducing the accessibility of active Pd sites[57].

To quantitatively assess the effect of surface reconstruction on the reactivity of Pd sites, the W values of Pd NPs were correlated with the TOF values of the Pd/CeO_2-T_{calc} series (Fig. 4b). As Pd NPs adopted flatter configurations, the intrinsic catalytic activity for MBY semi-hydrogenation increased, showing a clear linear scaling relationship (R^2 = 0.94). The intrinsic activity for optimal Pd/CeO_2-500 increased by 1.5-fold and 18.2-fold compared to the uncalcined one and Lindlar catalyst, respectively[38,39]. Notably, the TOF values of the catalysts

https://doi.org/10.1038/s41467-026-70568-z

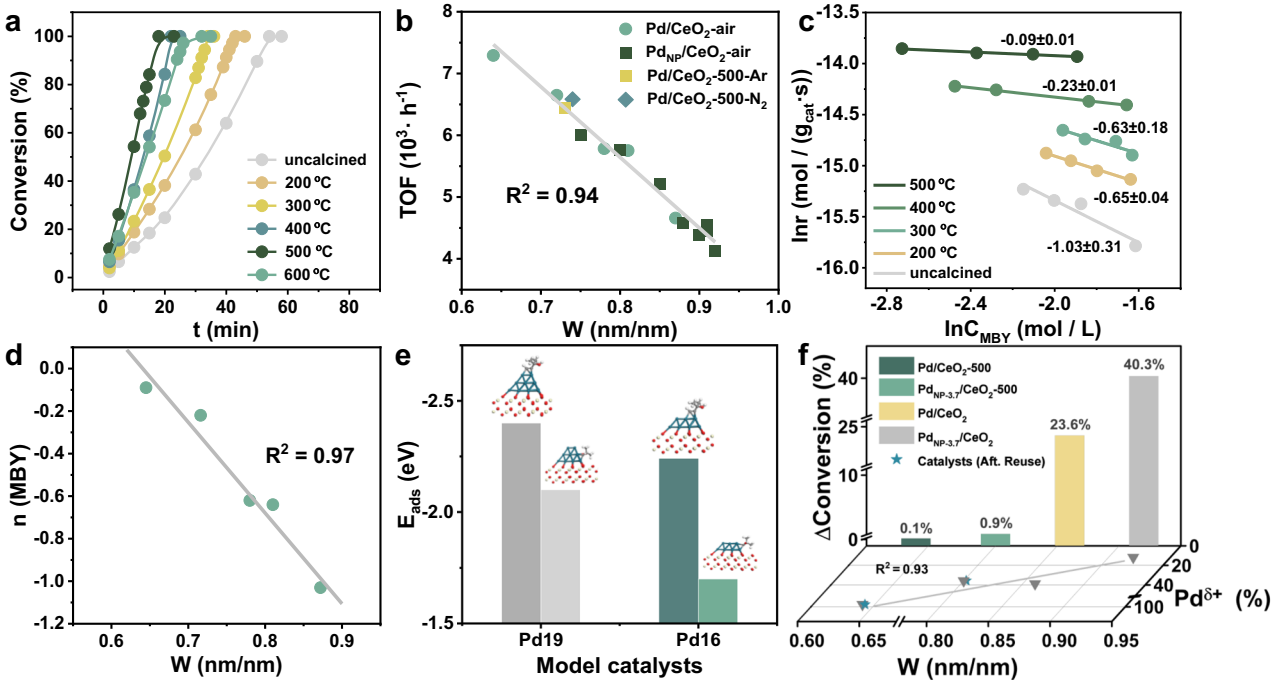

Fig. 4 | Influence of reconstruction on the activity of Alkyne Semi-Hydrogenation on Pd/CeO_2. **a** Catalytic performance of the semi-hydrogenation of MBY over the Pd/CeO_2-T_{calc} catalyst series. Reaction conditions: 1.02 mmol MBY, 20 mg catalyst, 5 mL ethanol, 35 °C, 1 bar H_2, 1000 rpm. **b**, **d** Correlation between W values of Pd species and the catalytic performance and reaction orders for MBY over the Pd/CeO_2 catalyst series. **c** Reaction orders of MBY over the Pd/CeO_2 catalysts. **e** Adsorption energies of MBY on different sites of Pd_{19}/CeO_2 and Pd_{16}/CeO_2. **f** Three-dimensional plot depicting the relationship among $Pd^{\delta+}$, W value, and cycling stability (conversion difference after 5 cycles) for Pd/CeO_2-500, Pd/CeO_2-uncalcined, $Pd_{NP\text{-}3.7}/CeO_2$-500, and $Pd_{NP\text{-}3.7}/CeO_2$-uncalcined catalysts; X/Y axes are W value and $Pd^{\delta+}$ content, respectively, and Z axis is conversion difference.

calcined in inert atmospheres for MBY semi-hydrogenation also fit within this linear scaling relationship (Fig. 4b, Supplementary Fig. 24). This suggests that this linear relationship may be independent of the concrete catalyst preparation processes or methods, displaying unexpected universality. Therefore, the W value can be used as an effective descriptor for predicting the intrinsic catalytic activity of MBY semi-hydrogenation on reconstructed Pd active sites.

The physicochemical origin of the W-value-dependent activity in MBY semi-hydrogenation over Pd/CeO_2 catalysts is elucidated through reaction order analysis[38,62]. As shown in Fig. 4c, the negative reaction order (n) of MBY gradually increased with rising calcination temperature. Specifically, the reaction order of MBY on Pd/CeO_2-500 (−0.09) increased by 91% compared to that on the uncalcined Pd/CeO_2 catalyst (−1.03). These results indicate that thermally induced Pd reconstruction effectively reduces the self-poisoning effect of MBY on Pd sites, thereby increasing the availability of surface Pd sites for hydrogenation, and finally may be beneficial for the enhanced intrinsic hydrogenation activity (TOF). A similar phenomenon was also observed for the hydrogen reaction order (n_{H_2}) as shown in Supplementary Fig. 25, with a slight increase from 1.31 to 1.87 accordingly. Though the higher n_{H_2} value suggests more kinetically demanding for hydrogen activation on the calcined catalyst, the overall increased hydrogenation activity demonstrates that the positive impact of weakened MBY self-poisoning outweighs the unfavorable factors that complicate hydrogen activation. This deduction is further testified by correlating the MBY reaction orders of the Pd/CeO_2-T_{calc} series with the corresponding W values (Fig. 4d, Supplementary Fig. 25), which also shows a clear linear scaling relationship ($R^2 = 0.97$). Pd NPs with lower W values or flatter shapes display smaller MBY reaction orders and exhibit weaker self-poisoning effect of MBY. Based on the XPS results of the Pd/CeO_2-T_{calc} series (Fig. 2j), the rise of the negative reaction orders may be well attributed to the increase in $Pd^{\delta+}$ sites after Pd reconstruction. As the *d*-π^* back-donation of shared electrons between electron-deficient Pd and C ≡ C is expected to weaken, the increase in electron-deficient $Pd^{\delta+}$ sites ultimately will reduce the overall adsorption strength of MBY on Pd sites[63,64]. To verify this, we constructed Pd_{19}/CeO_2 and Pd_{16}/CeO_2 models with three and two layers of Pd atoms, respectively, to simulate initial and calcined Pd active sites (Fig. 4e, Supplementary Fig. 26). DFT calculations showed that the adsorption energies of MBY decreased significantly after reconstruction, whether on top Pd sites or interfacial $Pd^{\delta+}$ sites, consistent with the previous deduction.

As reflected by the TOF-W linear relationship, the above rules also appear to be independent of the Pd precursor form. Supplementary Fig. 27 shows that the impact of thermally induced surface reconstruction on the activity of Pd_{NP}/CeO_2 catalysts for MBY semi-hydrogenation follows the same pattern as for Pd/CeO_2-T_{calc}, albeit to a lesser extent, primarily due to the lower flattening of Pd NPs under the same calcination conditions. The stability of Pd/CeO_2 can also be improved by thermally induced surface reconstruction. As shown, even after five cycles, the losses in catalytic activity and selectivity for both Pd/CeO_2-500 and $Pd_{NP\text{-}3.7}/CeO_2$-500 were negligible, while uncalcined Pd/CeO_2 and $Pd_{NP\text{-}3.7}/CeO_2$ catalysts suffered from significant deactivation (Supplementary Figs. 28–32). HRTEM analysis suggests that this deactivation may be due to significant Pd nanoparticle agglomeration.

To further clarify the intrinsic correlation between catalyst stability and Pd structural characteristics, we summarized the relationships among $Pd^{\delta+}$ content, W value, and cycling stability of Pd/CeO_2-500, Pd/CeO_2-uncalcined, $Pd_{NP\text{-}3.7}/CeO_2$-500, and $Pd_{NP\text{-}3.7}/CeO_2$-uncalcined catalysts as shown in Fig. 4f. The Pd morphological parameter W quantifies the degree of particle deformation, and cycling stability is measured by the difference in conversion rate before and after five cycles. Catalysts with a low initial W value (0.6–0.8) demonstrate negligible activity loss and constant Pd particle W values after five

cycles (Fig. 4f). This is due to a strong metal-support interaction, where electron transfer from Pd to CeO_2 increases the $Pd^{\delta+}$ population and flattens the Pd particles, yielding a smaller W value. Consequently, a lower W value reliably predicts better stability. In contrast, uncalcined $Pd_{NP\text{-}3.7}/CeO_2$ and Pd/CeO_2 catalysts, with W values approaching 1, suffer from weak interaction and inferior stability, as shown by the activity decline after five cycles from 89.6% to 49.3% and from 96.7% to 73.1%, respectively.

Decoupling electronic and geometric effects mediated by surface reconstruction

It is widely recognized that the selectivity regulation in the structurally sensitive MBY semi-hydrogenation reaction is more challenging. The most critical challenge here is that the current catalyst structure regulation methods struggle to decouple electronic and geometric effects, resulting in uncertainty about their individual impacts on selectivity[36]. This is evident in Fig. 5a, where W values and the ratio of $Pd^{\delta+}$ change simultaneously. To address this issue, we previously used a colloidal method to prepare supported Pt NPs with uniform size and morphology for the selective hydrogenation of halogenated nitrobenzenes[32]. The electronic structure of the Pt active phase was modulated using only the work functions of different supports, avoiding interference from geometric structures. This yielded a structure–performance relationship curve containing only electronic effects of supports. Based on the orthogonality of electronic and geometric effects in mathematical physics, we established a Cartesian coordinate system to decouple and quantify these two effects[32]. However, we found that Pd sites did not show significant electronic structure changes on different supports after low-temperature $NaBH_4$/tert-butylamine treatment, indicating that this strategy was not applicable to Pd catalyst systems.

To systematically uncover the regulatory role of thermally induced reconstruction and redispersion of Pd NPs on reaction selectivity, we used the Pd_{NP}/CeO_2-T_{calc} catalyst system, prepared with colloidal Pd NPs of varying sizes as precursor to ensure better control over initial variables[32]. To obtain sufficient data on catalyst structure and reaction performance, we also varied the calcination temperature in the Pd_{NP}/CeO_2-T_{calc} system (where T_{calc} denotes the calcination temperature). Catalysts with different initial Pd particle sizes are represented by different colored points and curves. Based on these results, we constructed a $Pd^{\delta+}$–W–Sel. three-dimensional relationship diagram, as shown in Supplementary Fig. 33. In the W–($Pd^{\delta+}$) plane, results indicated that the W values of Pd NPs on catalysts prepared under different conditions exhibited a clear positive linear scaling relationship with the ratio of $Pd^{\delta+}$ ($R^2 = 0.92$) (Fig. 5a). This linear correlation suggests that changes in the geometric and electronic structures of the Pd active phase during reconstruction are actually linearly constrained.

In the W–Sel. plane, the yellow points and curve in Fig. 5a illustrate the selectivity variation pattern of Pd_{NP}/CeO_2-T_{calc} with an initial size of 2.9 nm colloidal Pd NPs at various calcination temperatures. Below 300 °C, the selectivity of the catalyst for MBE increased significantly with rising calcination temperature. Then it remained between 96.5% and 97.2% when further raising the calcination temperature. A similar trend was observed for the selectivity of Pd_{NP}/CeO_2-T_{calc} with other colloidal Pd NPs of the same initial size, achieving the highest MBE selectivity exceeding 97.5% (Fig. 5a). Comparing the differences in selectivity among Pd_{NP}/CeO_2-T_{calc} catalysts of varying Pd sizes, it is evident that smaller Pd NPs on CeO_2 show a more significant improvement in MBE selectivity after air calcination. The five data curves, representing initial Pd particle sizes from 2.9 to 7.8 nm, form a two-dimensional contour plot that illustrates how MBE selectivity changes with the W value on Pd_{NP}/CeO_2-T_{calc} catalysts. Along the W axis, this interval can be divided into a plateau region with high selectivity and a steep region with rapidly decreasing selectivity (Fig. 5a). Taking the yellow curve of $Pd_{NP\text{-}2.9}/CeO_2$-T_{calc} as an example, the selectivity was in the plateau region when the W value was below 0.85, but fell into the rapidly decreasing steep region when the W value exceeded 0.85. As the initial Pd particle size increases, the W-value threshold for the plateau region shifts slightly to the right.

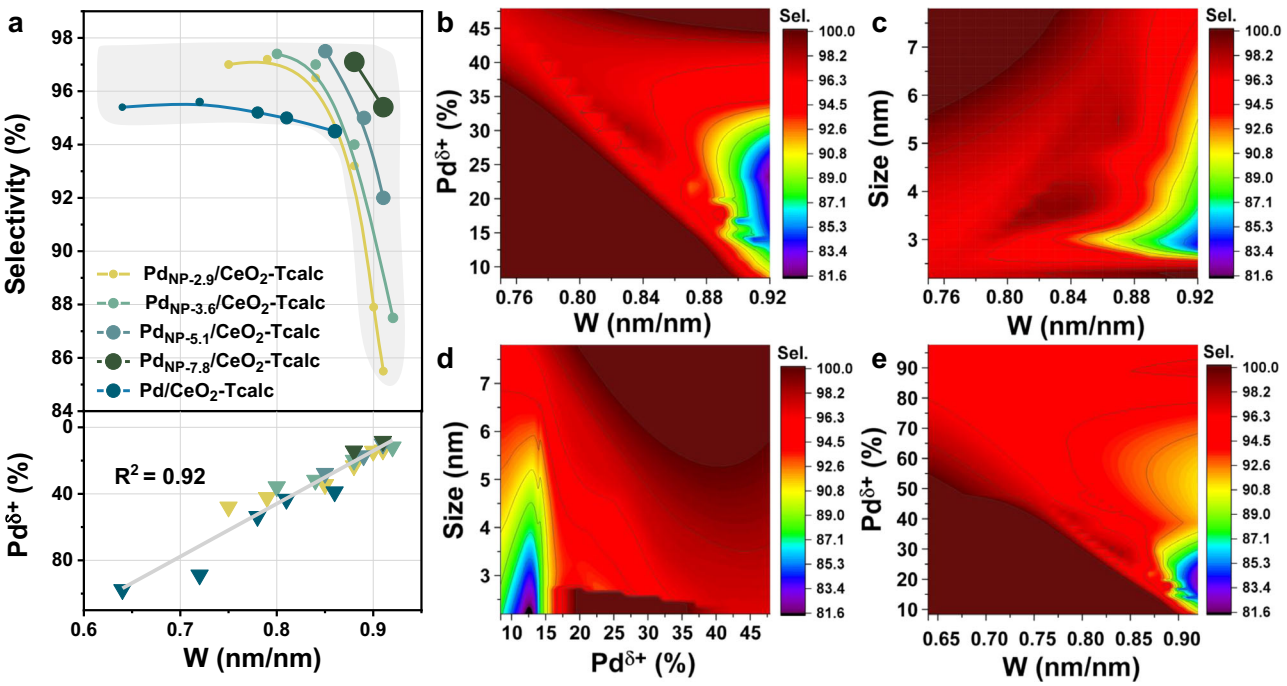

Fig. 5 | Structure–performance relationships in the Pd/CeO_2 catalysts series. **a** Linearly constrained relationship between the geometric (W) and electronic ($Pd^{\delta+}$) structures of the Pd active phase during reconstruction. **b** Correlation between the W values of Pd NPs and MBE selectivity. **c** W–($Pd^{\delta+}$)–selectivity, **d** W–size–selectivity, and **e** ($Pd^{\delta+}$)–size–selectivity contour maps for MBY selective hydrogenation on Pd_{NP}/CeO_2-T_{calc} catalysts. **f** W–($Pd^{\delta+}$)–selectivity contour map extended to catalysts prepared from $PdCl_2$ precursor.

In the plateau region, the W value showed significant variation. Following the Wulff construction principle, the geometric structure of Pd NPs experienced substantial deformation[65]. Concurrently, the electronic structure of Pd NPs also underwent considerable change due to the linear relationship between geometric and electronic structure evolution during surface reconstruction. As indicated by the Pd 3*d* XPS results in Supplementary Fig. 34, the surface Pd sites in the plateau region were generally electron-deficient. Consequently, the ongoing evolution of the electronic and geometric structures of Pd sites had minimal impact on reaction selectivity, given the pronounced electron-deficient state of Pd. In essence, the high selectivity of the catalyst for MBE in this range was primarily determined by the electron-deficient state of Pd sites, despite the C ≡ C bond semi-hydrogenation being a geometrically sensitive reaction[66]. According to Wulff Construction rules, the proportion of such low-coordinated sites as edge and corner sites on Pd particle surfaces gradually increases with the rise of the W value[65,67]. Plenty of research results have shown that these low-coordinated Pd sites, which have strong olefin adsorption capacity, often lead to over-hydrogenation side reactions, significantly reducing olefin selectivity[68]. Therefore, the constant MBE selectivity with W value in the plateau region could be regarded as a support for electronic effects on Pd sites. In the steep region, electron-rich Pd sites suggested the weak regulation of the electronic structure of Pd NPs by the CeO_2 support. At this stage, the geometric structure evolution of Pd NPs started to significantly influence selectivity, aligning with prior research findings. As can be seen in Fig. 5a, the MBE selectivity showed significant variation on Pd_{NP}/CeO_2-T_{calc} catalysts (T_{calc} <300 °C) with different particle sizes, despite their similar W values. According to Wulff construction rules, the selectivity change at this stage was mainly caused by different proportions of low-coordinated sites, like edge and corner atoms on the surfaces of Pd NPs with different sizes or morphologies[69].

It is crucial to note that the above rules for regulating alkyne hydrogenation activity and selectivity through thermally induced active component reconstruction proved effective with various active component precursors and reducible supports, showcasing a degree of universality. For instance, Pd/CeO_2-T_{calc} catalysts prepared using $PdCl_2$ as the precursor maintained consistently high selectivity after air calcination pretreatment at various temperatures (Supplementary Fig. 35).

This phenomenon can be explained by the electronic and geometric structures of the Pd sites being in the plateau region, as shown in Fig. 5a. Similarly, these conclusions also account for the high MBE selectivity of Pd/TiO_2-500 and Pd_{NP}/TiO_2-500 catalysts, as well as the serious over-hydrogenation side reaction on Pd/Al_2O_3, Pd/Al_2O_3-500, Pd/MgO, Pd/MgO-500, and Pd/SiO_2 catalysts (Supplementary Figs. 36, 37, Table 3).

Further processing of the three-dimensional data in Supplementary Fig. 32 through matrix transformation and grid interpolation yields the corresponding contour plots. These contour plots provide more detailed insights into the structure-activity relationship trends. For Pd_{NP}/CeO_2-T_{calc}-derived data (Fig. 5b), it is evident that the Pd/CeO_2 system exhibits severe over-hydrogenation only in a small region of the electronic–geometric parameter space (right portion of the plot). In other words, the Pd/CeO_2 system possesses exceptionally broad tunability in both electronic and geometric structures for achieving highly selective hydrogenation of alkynes. For small-sized supported Pd NPs, surface-reconstruction-induced flattening significantly expands the parameter space for high alkene selectivity (Fig. 5c). As long as the W value remains below 0.85, all Pd/CeO_2 catalysts exhibit desirable MBE selectivity. Moreover, this flattening effect appears more pronounced for supported Pd NPs smaller than 3 nm, effectively addressing the challenge of alkene selectivity control on small Pd clusters and substantially improving Pd atom utilization. Concurrently, over-hydrogenation side reactions on small supported Pd NPs are confined to highly electron-rich states ($Pd^{\delta+}$ < 15%) (Fig. 5d). Since small supported Pd NPs often experience significant electron transfer with reducible oxide supports, their electronic structures readily meet the requirements for high alkene selectivity when supported on strongly interacting reducible oxides[70]. Notably, when the sizes of Pd NPs are <3 nm, the flattening effect from surface reconstruction indicates that Pd in a relatively electron-rich state (18% < $Pd^{\delta+}$ < 37%) exhibits higher alkene selectivity compared to Pd sites nearby with other electronic configurations (Fig. 5d). It is crucial to emphasize that these trends are consistent regardless of the Pd precursors used. Data from catalysts prepared with $PdCl_2$ as a precursor did not significantly change the $Pd^{\delta+}$–W–Sel. contour-plot trends (Fig. 5e). Instead, the additional data enhanced the reliability and accuracy of alkene selectivity predictions. For instance, the overestimated selectivity (Sel. > 99%) in the upper-right region of Fig. 5b was corrected to a more reasonable range of 92–96%.

Thermally induced surface reconstruction of Pd/CeO_2 yields a high-performance, additive-free catalyst for alkyne semi-hydrogenation, achieving 97.5% olefin selectivity with 18.2-fold higher activity than Lindlar catalysts. Mechanistic studies reveal that oxidative redistribution of Pd nanoparticles into flattened, electron-deficient structures enhances metal-support interactions while suppressing over-hydrogenation. A geometric descriptor (W, flattening degree) and electronic descriptor $Pd^{\delta+}$ content) uncouple structure-activity relationships: TOF decreases linearly with W, whereas selectivity transitions at W = 0.85 from electronic-dominated ($Pd^{\delta+}$) to geometric-dominated (Pd^0) regimes. In addition, surface reconstruction drastically shrinks the electronic-geometric space of Pd sites for the over-hydrogenation side reaction. This work offers a unified approach for decoupling structure-sensitive effects in supported noble metal catalysts on reducible oxides. This approach is theoretically generalizable across such systems and may enable quantitative separation of electronic and geometric contributions in other structure-sensitive reactions.

Methods

Chemicals and materials

The subsequent chemicals were procured commercially and utilized as received, devoid of any additional treatment: palladium chloride ($PdCl_2$, 99.9%, 60.0 wt.% Pd), Cerium oxide (99.95%), 2-methyl-3-butyn-2-ol (MBY, AR), 2-methyl-3-buten-2-ol (MBE, AR), all sourced from Aladdin Industrial Corporation.

Synthesis of catalysts

Pd/CeO_2-T_{calc} nanocatalysts were synthesized using the conventional wetness impregnation method, with a nominal metal loading of 0.5 wt.%. The commercial cerium oxide supports underwent pretreatment at 500 °C for 4 h under pure H_2 (heating rate: 10 °C·min^{-1}) before utilization. In brief, a 252 µL $PdCl_2$ aqueous solution (containing 6 mg·mL^{-1} Pd) was dissolved in 20 mL of deionized water. Subsequently, 300 mg of cerium oxide was slowly added to the solution with continuous magnetic stirring at 50 °C for 10 h. Following impregnation, the samples were calcined in static air at temperatures ranging from 200 to 600 °C for 4 h (heating rate: 5 °C·min^{-1}). The resulting yellow solids were then subjected to reduction in pure H_2 atmosphere at 200 °C for 1 h, employing a heating rate of 2 °C·min^{-1}, yielding the Pd/CeO_2-T_{calc} catalysts (where T_{calc} denotes the calcined temperature). Similarly, 5 Pd/CeO_2 was synthesized by adjusting the quantity of the metal precursor. Pd/CeO_2-500-N_2 and Pd/CeO_2-500-Ar were prepared using the same synthetic approach, with the exception of calcination under pure N_2 or Ar environment.

The synthetic approach for generating Pd nanoparticles (NPs) was refined based on a previously reported method[24], subsequently involving wetness impregnation and air calcination at 500 °C to fabricate the series Pd_{NP}/CeO_2-500 catalysts with varying particle sizes. The removal of the capping agent (polyvinyl pyrrolidone, PVP) from

the surface of PVP-Pd_{NP}/CeO_2 catalysts was executed using a $NaBH_4$/tert-butylamine (TBA) aqueous solution, following the established procedures. In a typical procedure, the as-prepared PVP-Pd_{NP}/CeO_2 catalysts were treated in 6.2 mL $NaBH_4$/TBA solution (TBA: H_2O: $NaBH_4$ = 5 mL: 1.2 mL: 10 mg) under continuous stirring for 1 h in ice baths, following by separation through centrifugation. The collected samples were then washed with acetone three times to remove the surface amines. After drying in a vacuum at 60 °C overnight, a series of Pd_{NP}/CeO_2 catalysts with different particle sizes was successfully obtained.

Characterizations

High-resolution transmission electron microscopy (HRTEM), high-angle annular dark field scanning transmission electron microscopy (HAADF-STEM), and elemental mapping with energy dispersive X-ray spectroscopy (EDS) tests were conducted on the JEOL JEM-2100F at an acceleration voltage of 200 kV. To ensure the accuracy and reliability of the W descriptor (defined as the ratio of the shortest diameter (R1) to the longest diameter (R2) of the two-dimensional projection of Pd clusters, characterizing the degree of particle deformation, Fig. 1e), the following measurement restrictions were implemented: (i) Since TEM images reflect two-dimensional projections, only Pd particles attached to the edge of the support were selected as statistical objects to avoid the influence of support contrast on Pd particle measurement; (ii) To reduce accidental errors, the number of Pd particles for statistics was increased as much as possible, so that the full width at half maximum (FWHM) of the W parameter distribution was lower than 0.20, thereby ensuring the coefficient of determination (R^2) of the linear scaling relationship ≥ 0.95. For each catalyst sample, the average W value of Pd particles was obtained through statistical analysis of at least 60 Pd particles. For example, the W value of the Pd/CeO_2-500 catalyst was obtained by statistical analysis of 112 Pd particles. Environmental transmission electron microscopy analysis was carried out on the Hitachi H-9500 (300 kV) at 4.5×10^{-2} Pa under an oxygen atmosphere. Power X-ray diffraction (XRD) was measured in a Rigaku Ultima IV operating at 40 kV and 20 mA with Cu Kα radiation. The data was recorded in the 20°–80° 2θ range. The N_2 adsorption-desorption isothermal analysis was performed using a Micromeritics ASAP 2020 HD88. The Brunauer-Emmett-Teller (BET) method was applied to estimate the total surface area, S_{BET}. The metal loading of the catalysts was determined by the inductively coupled plasma mass spectrometry (ICP-MS) using a PerkinElmer NexION 2000 equipment. Temperature-programmed reduction with hydrogen (H_2-TPR) was conducted in a FINESORB-3010 apparatus equipped with a thermal conductivity detector (TCD). The X-ray photoelectron spectra (XPS) were obtained on an ESCALAB MARK II spherical analyzer with an aluminum anode (1486.6 eV) X-ray source, calibrated by the C 1*s* peak (284.8 eV). Pulsed CO chemisorption was conducted on a FINESORB-3010 apparatus to determine the dispersion of Pd in the catalyst. The samples (approximately 100 mg) were loaded in a U-shaped quartz reactor between two plugs of quartz wool, which were purged for 1 h with He at 150 °C to remove the vapor and impurities. When the sample was cooled to room temperature, the pulse CO chemisorption test was then conducted with 50 vol% of CO in He.

Catalytic test

The semi-hydrogenation of MBY was evaluated under atmospheric pressure using a 50 mL three-necked round-bottom flask. For each reaction, 20 mg Pd/CeO_2-T_{calc} and 100 µL substrate were thoroughly dispersed in 5 mL of ethanol, and the mixture was exposed to a hydrogen-filled balloon (1 bar). Prior to initiating the reaction, the flask underwent five cycles of hydrogen purging to eliminate any air present. During the reaction proceeding, samples were intermittently withdrawn using a syringe and subjected to analysis using gas chromatography-flame ionization detector (GC-FID). The resulting products were further characterized through gas chromatography-mass spectrometry (GC-MS). The turnover frequency (TOF) was calculated using the formula: TOF = (mol of alkynes × conversion) / (mol of surface-exposed Pd atoms × reaction time), conversion ≤ 10%.

For the $Pd^{\delta+}$–W–selectivity contour mapping, the commercially available software Origin, which is widely used in the research field, was employed for matrix transformation and grid interpolation. The grid interpolation adopted the Random (Renka-Cline) method, and the data smoothing standard reached C1 continuity (first-order differentiable). Other settings, such as grid density, adopted the default parameters of Origin software, which were consistent with the conventional operation standards in the related research field.

Cycling stability test

The reaction blend comprising 20 mg of Pd/CeO_2-500 and 100 µL of substrate was dispersed within 5 mL of ethanol. The solution was subjected to vigorous stirring (1000 rpm) at 35 °C under 1 bar H_2. The reaction was halted after a predetermined duration, subsequent to which the catalysts were separated through centrifugation. The utilized catalysts underwent a thorough washing procedure with ethanol, involving three successive washes, before being dried under vacuum conditions at 60 °C overnight, in preparation for the cycling stability assessment.

Density functional theory calculations

Calculations were performed by using periodic, spin-polarized DFT as implemented in the Vienna ab initio program package (VASP, version 6.1), using the projector augmented wave (PAW) method proposed by Blöchl and implemented by Kresse. A cutoff energy of 400 eV for plane waves was set through all the calculations. The exchange correlation energy was modeled by using the Perdew-Burke-Ernzerhof (PBE) functional within the generalized gradient approximation (GGA). Pd nanoparticles with 49 atoms (Pd49) were established based on the Wulff construction. A p(6 × 6) supercell with six atomic layers containing 214 atoms for the CeO_2 model was constructed, and two of the surface oxygen atoms were removed to simulate the oxygen vacancies. A k-point of 2 × 2 × 1 was used for the Brillouin zone sampling for structure optimization. The periodic condition was employed along the x and y directions, and the vacuum region between the slabs was 15 Å, which is sufficiently large to keep spurious interactions negligible. The upper three-layer atoms for CeO_2 in the supercells were allowed to relax. Meanwhile, the bottom three-layer atoms were fixed during the AIMD simulation. The geometry optimization was stopped when the force residue on the atom was smaller than 0.02 eV·Å^{-1}, and the energy difference was <10^{-4} eV.

Data availability

The data that support the findings of this study can be found in the manuscript and Supplementary information, or are available from the corresponding author upon request.

References

1. Tao, F. & Salmeron, M. Surface restructuring and predictive design of heterogeneous catalysts. *Science* **386**, eadq0102 (2024).
2. Zhang, L., Zhou, M., Wang, A. & Zhang, T. Selective hydrogenation over supported metal catalysts: from nanoparticles to single atoms. *Chem. Rev.* **120**, 683–733 (2020).
3. Macino, M. et al. Tuning of catalytic sites in Pt/TiO_2 catalysts for the chemoselective hydrogenation of 3-nitrostyrene. *Nat. Catal.* **2**, 873–881 (2019).
4. Yamada, Y. et al. Nanocrystal bilayer for tandem catalysis. *Nat. Chem.* **3**, 372–376 (2011).
5. Wang, Y. et al. Visualizing element migration over bifunctional metal-zeolite catalysts and its impact on catalysis. *Angew. Chem. Int. Ed.* **60**, 17735–17743 (2021).

6. Yuan, Q. et al. Ordered mesoporous Ce_1–xZr_xO_2 solid solutions with crystalline walls. *J. Am. Chem. Soc.* **129**, 6698–6699 (2007).
7. Vilé, G. et al. A stable single-site palladium catalyst for hydrogenations. *Angew. Chem. Int. Ed.* **54**, 11265–11269 (2015).
8. Lin, R. et al. Cover picture: design of single gold atoms on nitrogen-doped carbon for molecular recognition in alkyne semi-hydrogenation. *Angew. Chem. Int. Ed.* **58**, 351–351 (2019).
9. Wang, Z. et al. Synthesis of Pd nanoframes by excavating solid nanocrystals for enhanced catalytic properties. *ACS Nano* **11**, 163–170 (2017).
10. Zhang, T. et al. Unconventional route to encapsulated ultrasmall gold nanoparticles for high-temperature catalysis. *ACS Nano* **8**, 7297–7304 (2014).
11. Luo, Z. et al. Transition metal-like carbocatalyst. *Nat. Commun.* **11**, 4091 (2020).
12. Guo, Y. et al. Low-Temperature CO_2 methanation over CeO_2-supported ru single atoms, nanoclusters, and nanoparticles competitively tuned by strong metal–support interactions and H-spillover effect. *ACS Catal.* **8**, 6203–6215 (2018).
13. Morgan, K., Goguet, A. & Hardacre, C. Metal redispersion strategies for recycling of supported metal catalysts: a perspective. *ACS Catal* **5**, 3430–3445 (2015).
14. Wanke, S. E. Sintering and redispersion of conventional supported metal catalysts in hydrogen and oxygen atmospheres. *Mater. Sci. Res.* **16**, 223–242 (1984).
15. Yang, X. et al. Taming the stability of Pd active phases through a compartmentalizing strategy toward nanostructured catalyst supports. *Nat. Commun.* **10**, 1611 (2019).
16. Sá, J. et al. Influence of methyl halide treatment on gold nanoparticles supported on activated carbon. *Angew. Chem. Int. Ed.* **50**, 8912–8916 (2011).
17. Gollob, R. & Dadyburjor, D. B. Regeneration of model-supported metal catalysts. *J. Catal.* **68**, 473–486 (1981).
18. Gänzler, A. M. et al. Tuning the structure of platinum particles on ceria insitu for enhancing the catalytic performance of exhaust gas catalysts. *Angew. Chem. Int. Ed.* **56**, 13078–13082 (2017).
19. Luo, Z. et al. A microporous covalent–organic framework with abundant accessible carbonyl groups for lithium-ion batteries. *Angew. Chem. Int. Ed.* **57**, 9443–9446 (2018).
20. Colherinhas, G. & Fileti, E. Molecular description of surfactant-like peptide-based membranes. *J. Phys. Chem. C* **118**, 9598–9603 (2014).
21. Kaden, W. E. et al. Electronic structure controls reactivity of size-selected Pd clusters adsorbed on TiO_2 surfaces. *Science* **326**, 826–829 (2009).
22. Lei, H. et al. Thermally triggered redox flexibility of Pt/CeO_2 cluster catalyst against in-situ atomic redispersion. *Angew. Chem. Int. Ed.* https://doi.org/10.1002/anie.202509239 (2025).
23. Wang, F. et al. Identification of direct anchoring sites for monoatomic dispersion of precious metals (Pt, Pd, Ag) on CeO_2 support. *Angew. Chem. Int. Ed.* **63**, e202318492 (2024).
24. Vilé, G., Bridier, B., Wichert, J. & Pérez-Ramírez, J. Ceria in hydrogenation catalysis: high selectivity in the conversion of alkynes to olefins. *Angew. Chem. Int. Ed.* **51**, 8620–8623 (2012).
25. Sankar, M. et al. Role of the support in gold-containing nanoparticles as heterogeneous catalysts. *Chem. Rev.* **120**, 3890–3938 (2020).
26. Mitchell, S. & Pérez-Ramírez, J. Atomically precise control in the design of low-nuclearity supported metal catalysts. *Nat. Rev. Mater.* **6**, 969–985 (2021).
27. Hu, J. et al. Sulfur vacancy-rich MoS_2 as a catalyst for the hydrogenation of CO_2 to methanol. *Nat. Catal.* **4**, 242–250 (2021).
28. Zhou, H. et al. Recover the activity of sintered supported catalysts by nitrogen-doped carbon atomization. *Nat. Commun.* **11**, 335 (2020).
29. Lambrou, P. S., Polychronopoulou, K., Petallidou, K. C. & Efstathiou, A. M. Oxy-chlorination as an effective treatment of aged Pd/CeO_2-Al_2O_3 catalysts for Pd redispersion. *Appl. Catal. B: Environ.* **111–112**, 349–359 (2012).
30. Chen, Z.-Y., Yuan, C., Zhang, H., Zhang, X. & Zhou, Z. Stimuli-responsive coinage metal nanoclusters. *Coord. Chem. Rev.* **543**, 216930 (2025).
31. Kang, S.-Y., Nan, Z.-A. & Wang, Q.-M. Superatomic orbital splitting in coinage metal nanoclusters. *J. Phys. Chem. Lett.* **13**, 291–295 (2022).
32. Wang, Z. et al. Decoupling the electronic and geometric effects of Pt catalysts in the selective hydrogenation reaction. *Nat. Commun.* **13**, 3561 (2022).
33. Bhaskar, G. et al. Breaking new ground: MBene route toward selective vinyl double bond hydrogenation in nitroarenes. *J. Am. Chem. Soc.* **145**, 27459–27470 (2023).
34. Li, Y. et al. Direct conversion of carbon dioxide into liquid fuels and chemicals by coupling green hydrogen at high temperature. *Appl. Catal. B: Environ.* **324**, 122299 (2023).
35. Wang, D.-J. et al. Tuning selectivity of CO_2 hydrogenation via support composition modification adjusted the activity reduction of H species over $Ce1–xPr_xO_2–\delta$-supported metal (Ru, Rh) nanoclusters. *ACS Catal.* **14**, 10060–10076 (2024).
36. Shen, L. et al. PdZn intermetallic on a CN@ZnO hybrid as an efficient catalyst for the semihydrogenation of alkynols. *J. Catal.* **350**, 13–20 (2017).
37. Wang, Z. et al. Fundamental aspects of alkyne semi-hydrogenation over heterogeneous catalysts. *Nano Res.* **15**, 10044–10062 (2022).
38. Boitiaux, J. P., Cosyns, J. & Vasudevan, S. Hydrogenation of highly unsaturated hydrocarbons over highly dispersed palladium catalyst: Part I: behaviour of small metal particles. *Appl. Catal.* **6**, 41–51 (1983).
39. Xiong, J. et al. Mediating trade-off between activity and selectivity in alkynes semi-hydrogenation via a hydrophilic polar layer. *Nat. Commun.* **15**, 1228 (2024).
40. Brunauer, S., Emmett, P. H. & Teller, E. Adsorption of gases in multimolecular layers. *J. Am. Chem. Soc.* **60**, 309–319 (1938).
41. Blanco, J. M. et al. Origin of contrast in STM images of oxygen on Pd(111) and its dependence on tip structure and tunneling parameters. *Phys. Rev. B* **71**, 113402 (2005).
42. Fu, Q., Saltsburg, H. & Flytzani-Stephanopoulos, M. Active nonmetallic Au and Pt species on ceria-based water-gas shift catalysts. *Science* **301**, 935–938 (2003).
43. Komai, S. et al. Determination of metal dispersion of Pt/CeO_2 catalyst by the CO-pulse method. *J. Jpn. Pet. Inst.* **48**, 173–177 (2005).
44. Boudart, M. & Hwang, H. S. Solubility of hydrogen in small particles of palladium. *J. Catal.* **39**, 44–52 (1975).
45. Pinna, F., Signoretto, M., Strukul, G., Polizzi, S. & Pernicone, N. Pd-SiO_2 catalysts. Stability of β-PdHx as a function of Pd dispersion. *React. Kinet. Catal. Lett.* **60**, 9–13 (1997).
46. Niu, Y. et al. Visualizing formation of intermetallic PdZn in a palladium/Zinc oxide catalyst: interfacial fertilization by pdHx. *Angew. Chem. Int. Ed.* **58**, 4232–4237 (2019).
47. Pinna, F. et al. Consecutive hydrogenation of benzaldehyde over Pd catalysts: influence of supports and sulfur poisoning. *Appl. Catal. A: Gen.* **219**, 195–200 (2001).
48. Farmer, J. A. & Campbell, C. T. Ceria maintains smaller metal catalyst particles by strong metal-support bonding. *Science* **329**, 933–936 (2010).
49. Hansen, T. W., DeLaRiva, A. T., Challa, S. R. & Datye, A. K. Sintering of catalytic nanoparticles: particle migration or ostwald ripening? *Acc. Chem. Res.* **46**, 1720–1730 (2013).
50. Li, R. et al. In situ identification of the metallic state of Ag nanoclusters in oxidative dispersion. *Nat. Commun.* **12**, 1406 (2021).

51. Cargnello, M. et al. Control of metal nanocrystal size reveals metal-support interface role for ceria catalysts. *Science* **341**, 771–773 (2013).
52. Farrauto, R. J., Lampert, J. K., Hobson, M. C. & Waterman, E. M. Thermal decomposition and reformation of PdO catalysts; support effects. *Appl. Catal. B: Environ.* **6**, 263–270 (1995).
53. Luo, M.-F., Hou, Z.-Y., Yuan, X.-X. & Zheng, X.-M. Characterization study of CeO_2-supported Pd catalyst for low-temperature carbon monoxide oxidation. *Catal. Lett.* **50**, 205–209 (1998).
54. Nie, L. et al. Activation of surface lattice oxygen in single-atom Pt/CeO_2 for low-temperature CO oxidation. *Science* **358**, 1419–1423 (2017).
55. Bruix, A. et al. Maximum noble-metal efficiency in catalytic materials: atomically dispersed surface platinum. *Angew. Chem. Int. Ed.* **53**, 10525–10530 (2014).
56. Brun, M., Berthet, A. & Bertolini, J. C. XPS, AES and Auger parameter of Pd and PdO. *J. Electron Spectrosc. Relat. Phenom.* **104**, 55–60 (1999).
57. Slavinskaya, E. M. et al. Low-temperature CO oxidation by Pd/CeO_2 catalysts synthesized using the coprecipitation method. *Appl. Catal. B: Environ.* **166–167**, 91–103 (2015).
58. Wang, Z. et al. Dual Pd^{2+} and Pd^0 sites on CeO_2 for benzyl alcohol selective oxidation. *J. Catal.* **414**, 385–393 (2022).
59. Tauster, S. J., Fung, S. C., Baker, R. T. K. & Horsley, J. A. Strong Interactions in Supported-Metal Catalysts. *Science* **211**, 1121–1125 (1981).
60. Zou, X. et al. Core-shell PdO@SiO_2/Al_2O_3 with sinter-resistance and water-tolerance promoting catalytic methane combustion. *Chem. Eng. J.* **396**, 125275 (2020).
61. Huang, W., Zuo, Z., Han, P., Li, Z. & Zhao, T. XPS and XRD investigation of Co/Pd/TiO_2 catalysts by different preparation methods. *J. Electron. Spectrosc. Relat. Phenom.* **173**, 88–95 (2009).
62. Hungría, A. B., Calvino, J. J., Anderson, J. A. & Martínez-Arias, A. Model bimetallic Pd-Ni automotive exhaust catalysts: influence of thermal aging and hydrocarbon self-poisoning. *Appl. Catal. B: Environ.* **62**, 359–368 (2006).
63. Kubas, G. J. Metal–dihydrogen and σ-bond coordination: the consummate extension of the Dewar–Chatt–Duncanson model for metal–olefin π bonding. *J. Organomet. Chem.* **635**, 37–68 (2001).
64. Li, B. et al. Construction of Pd and PdCu alloy heterostructures for enhanced benzophenone hydrogenation performance. *Fuel* **388**, 134410 (2025).
65. Li, S. F., Zhao, X. J., Xu, X. S., Gao, Y. F. & Zhang, Z. Stacking principle and magic sizes of transition metal nanoclusters based on generalized wulff construction. *Phys. Rev. Lett.* **111**, 115501 (2013).
66. Crespo-Quesada, M., Yarulin, A., Jin, M., Xia, Y. & Kiwi-Minsker, L. Structure sensitivity of alkynol hydrogenation on shape- and size-controlled palladium nanocrystals: which sites are most active and selective? *J. Am. Chem. Soc.* **133**, 12787–12794 (2011).
67. Lykhach, Y. et al. Counting electrons on supported nanoparticles. *Nat. Mater.* **15**, 284–288 (2016).
68. Dai, Y. et al. Interface of biomolecular condensates modulates redox reactions. *Chem.* **9**, 1594–1609 (2023).
69. Decarolis, D. et al. Localized thermal levering events drive spontaneous kinetic oscillations during CO oxidation on Rh/Al_2O_3. *Nat. Catal.* **7**, 829–837 (2024).
70. Reiter, M. A. et al. A synthetic methylotrophic Escherichia coli as a chassis for bioproduction from methanol. *Nat. Catal.* **7**, 560–573 (2024).

Acknowledgments

Financial support from the National Natural Science Foundation of China (22325204 & 2247020015) and the "Pioneer" R&D Program of Zhejiang (2023C01108) is greatly appreciated.

Author contributions

M.L. performed the catalyst preparation, characterization, catalytic tests and calculations. M.L., Z.F. and Q.L. participated in the catalyst preparation and characterization. S.M. and B.L. provided helpful discussions. S.M., M.L. and Y.W. designed this study and analyzed the data. M.L., S.M. and Y.W. wrote the manuscript. Y.W. supervised the project. L.Z., S.L. and T.L. provided additional assistance to this work. All authors discussed the results and commented on the manuscript.

Competing interests

The authors declare no competing interests.

Additional information

Supplementary information The online version contains supplementary material available at https://doi.org/10.1038/s41467-026-70568-z.

Correspondence and requests for materials should be addressed to Yong Wang or Shanjun Mao.

Peer review information *Nature Communications* thanks Meenakshisundaram Sankar and the other anonymous reviewer(s) for their contribution to the peer review of this work. A peer review file is available.